TOF-PET image reconstruction with multiple timing kernels applied on Cherenkov radiation in BGO

Nikos Efthimiou (*Member IEEE*), Nicolaus Kratochwil, Stefan Gundacker, Andrea Polesel, Matteo Salomoni, Etiennette Auffray and Marco Pizzichemi

***Abstract*—Today Time-Of-Flight in PET scanners assumes a unique, well-defined timing resolution for all coincidence events. However, recent BGO-Cherenkov detectors, combining prompt Cherenkov emission and the typical BGO scintillation signal, are capable of sorting events into multiple mixture timing kernels and therefore increase the available information for the image reconstruction. The number of Cherenkov photons detected per event impacts directly the signal rise time, which can therefore be used to improve the timing resolution. In this work, we present a simulation toolkit that outputs data with multiple timing resolutions and image reconstruction that incorporates this information. A full cylindrical BGO-Cherenkov PET model was compared, in terms of contrast recovery and contrast-to-noise ratio, against non-TOF and an LYSO model with time resolution of 213 ps. Two reconstruction approaches for the mixture kernels were tested; mixture Gaussian and decomposed simple Gaussian models. The decomposed model used the exact mixture component applied in the simulation. Images reconstructed using mixture kernels provided similar mean value and less noise as compared to the decomposed simple Gaussian kernels. Although, the later converged faster. Related to the standard LYSO model, the BGO-Cherenkov provided similar contrast, although, in most cases, with more iterations. However, due to the higher sensitivity, the contrast-to-noise ratio was 26.4% better for the BGO model.**

***Index Terms*—PET, Time-of-Flight, BGO, Cherenkov, Mixture Gaussian model**

I. Introduction

TRADITIONAL image reconstruction of data acquired by Positron Emission Tomography (PET) scanners did not include timing information [1]. However, nowadays it is widely accepted that the incorporation of the Time-of-Flight (TOF) [2]–[5] information in the image reconstruction process provides better image properties and improved lesion detectability [6]–[13]. Therefore, manufacturers and researchers alike strive to achieve the best possible timing resolution [14]–[19].

The TOF benefits strongly depend on the timing resolution of the detectors, a crucial component of which is the scintillation crystal. Most scintillation crystals with good timing resolutions are based on the ^{176}Lu element [20]–[24]. Compared to $Bi_4Ge_3O_{12}$ (BGO), Lu-based crystals present better energy and timing properties, however, to the disadvantage of higher cost, lower stopping power and intrinsic radioactivity. Detailed comparison between Lu-based and BGO crystals has been presented in the past [25].

Recently, the exploitation of the prompt Cherenkov photons in BGO crystals and their potential benefits in the detection timing has sparked considerable scientific interest, as they provide the prospect of high sensitivity and compelling timing properties [26]–[36]. Cherenkov radiation is emitted when charged particles pass through a dielectric medium at speed greater than the phase velocity of light [37]. When measuring with a time-correlated single-photon counting setup and comparing the ratio of prompt light to scintillation light, about 17 ± 3 Cherenkov photons [38] are produced upon 511 keV excitation.

However, the number of detected Cherenkov photons underlies high fluctuations from *event-to-event* [38], [39]. Therefore, their detection does not provide a single timing resolution but rather a range, which depends on the ratio of BGO scintillation (slow) or Cherenkov photons (fast) detected [35]. Classification of the detected events in categories based on the above ratio results in the creation of a finite number of Gaussian kernels.

In this paper, we present the validation of a framework for statistical simulations of a mixture timing response of full PET scanners. In this instance, we used the above framework to approximate the timing performance of BGO-Cherenkov detectors effectively. Also, we explore the performance of a TOF reconstruction with single and multiple mixture timing kernels. Furthermore, we compare the performance of a BGO-Cherenkov scanner model with an LYSO model having a time resolution based on a currently available clinical scanner [40], [41]. Potential benefits in terms of Contrast Recovery Coefficient (CRC), Contrast-to-Noise Ratio (CNR) and noise on image quality using the proposed timing models are presented and discussed. Finally, we briefly discuss some challenges of the BGO-Cherenkov detectors at system level.

Nikos Efthimiou is with the Department Radiology, Perelman School of Medicine, University of Pennsylvania, USA, and with the PET Research Centre, Faculty of Health Sciences, University of Hull, Cottingham Rd, Hull, HU6 7RX, UK (contact: efthymin@pennmedicine.upenn.edu).

Nicolaus Kratochwil is with University of Vienna, Austria, and with European Organization for Nuclear Research, Geneve, Switzerland (CERN).

Stefan Gundacker, Andrea Polesel, Matteo Salomoni and Marco Pizzichemi are with University of Milano-Bicocca, Milano, Italy, and with European Organization for Nuclear Research, Geneve, Switzerland (CERN).

Etiennette Auffray is with European Organization for Nuclear Research, Geneve, Switzerland (CERN).

This work was initiated in the frame of COST Action TD1401 (FAST) and performed in the frame of the Crystal Clear Collaboration. We acknowledge the Viper High Performance Computing facility of the University of Hull and its support team. The authors would like to thank dr. S. Surti (Univ. of Pennsylvania, USA) and dr. C. Tsoumpas (Univ. of Leeds, UK) for the fruitful discussions and suggestions. Nikolaos Efthymiou was supported in part by NIH grant R21-CA239177.

II. Materials and Methods

A. Experimental determination of the TOF kernels

The timing properties of the BGO detectors were previously measured [39], [42]. In brief, $2 \times 2 \times 20$ mm^3 BGO crystals, wrapped in Teflon and optically coupled with Meltmount to 4×4 mm^2 FBK NUV-HD SiPMs were used to measure photon detection time differences from a ^{22}Na point source. The signals were readout by high-frequency electronics [42] and digitised by a LeCroy DDA735Zi oscilloscope with 3.5 GHz bandwidth and a sampling rate of 20 Gs s^{-1} for each of the four channels.

We recorded the scintillation pulse rise time of each channel for every event within an energy window of $440 - 665$ keV and measured an energy resolution of 19 % FWHM. The pulse rise times, between 10 mV and 50 mV, together with the coincidence time delay were stored and analysed offline. Events with a large number of detected Cherenkov photons had faster SiPM signal rises than when Cherenkov photons were not detected. This classification is illustrated on Fig. 1(top).

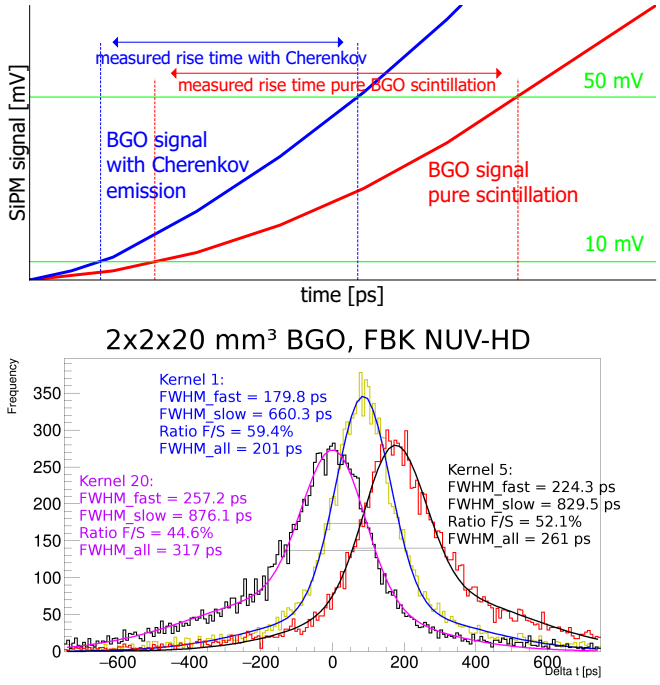

Fig. 1. (top:) The principle of the rise time separation: for events where only BGO scintillation is detected the SiPM signal rises slower (red) compared to the signal where Cherenkov photons are detected (blue) at the beginning of the signal. (bottom:) Time delay histogram with double Gaussian fit function for three types of categories.

We partitioned the events in 5 categories per detector. Each category contained 20% of the photopeak events (4% of the events in coincidence), based on the measured signal rise time. The distribution of the time delays coming from either BGO scintillation or Cherenkov photons was modelled with a double Gaussian function [38].

This formed a mixture model with two Gaussian components. The measured time resolution ranges from 201 ps FWHM (544 ps FWTM) to 333 ps FWHM (1109 ps FWTM), depending on the category. After time-walk correction the corresponding values are 288 ps FWHM (954 ps FWTM) before and 259 ps FWHM (891 ps FWTM) after correction, when merging all categories together [35]. The coincidence time delay of three of the categories is shown in Fig. 1(bottom). More details on the experimental measurement, analysis and results can be found in [35].

B. Simulation toolkit

We performed the scanner simulations on a modified GATE Monte Carlo (MC) simulation toolkit (v8.1) [43]. In particular, we changed the `GateTemporalResolution` and `GateCoincidenceSorter` classes. Originally, GATE applies the timing spread on each `single` γ-photon, individually, before the coincidence sorter. However, in order to accurately reproduce the measured timing kernels we applied the time spread in the `GateCoincidenceSorter`, a class that pairs the singles to coincidences.

For that, we generate a random number using a uniform Probability Density Function (PDF) and the `G4RandGeneral.shoot()` function. Based on this number we choose which of the 25 timing categories (rows of Table I) to apply on the event pair. Then, we generate a second random number, using the above method, which is compared with the abundance ratio (α_p) (Table I column 3) to choose either the fast or slow component. The selected time spread is applied on the two single timestamps selecting a random number from a Normal PDF with the specified distribution. Finally, before storage the pair is checked for coincidence.

1) Scanner Simulation models: All scanner models in this study have the same geometry, i.e. a generic cylindrical shape. They have 666 crystals per ring each with size of $4 \times 4 \times 20$ mm^3, arranged on 48 rings with axial length of $\approx$ 20 cm. The geometry was designed to be as close to a cylinder as possible, avoiding any blocks. The scanner models vary in crystal material, timing and energy properties, and coincidence window.

The BGO model was simulated as (a) `BGO-Ch` with a single Gaussian mixture timing spread of 179.8 ps and 660.3 ps (only first row of Table I), and (b) `BGO-mCh` with 25 mixture timing spreads, as summarised in Table I. The energy resolution was set to 19% and the coincidence window to 9 ns. The energy window was $425 - 650$ keV. The second model had LYSO crystals (density: 7.105 g.cm^{-3}), 11% energy and 213 ps timing resolution. The values approximate those reported for the Siemens Vision PET scanner [40], [41]. The coincidence window was 4 ns and the energy window was set to $450 - 650$ keV. The minimum radial distance for two singles to be considered for coincidence was set to 83 `r-sectors` (as defined in GATE).

We should note, that the BGO crystal profiles of the model are not the same as those in the experiment. It is expected that the crystal profile ($4 \times 4 \times 20$) will have slightly poorer timing properties. The deterioration with larger crystal cross section ($3 \times 3 \times 15$ instead of $2 \times 2 \times 15$) was measured to be about 8% [36].

2) Simulated Acquisition: We simulated 5 noise realisations of the NEMA Image Quality (IQ) phantom [44] with

TABLE I
TIMING CATEGORIES OF THE GAUSSIAN MIXTURE MODELS USED AT THE BGO−MCH MODEL. THE VALUES AT THE FIRST LINE WAS USED AT THE BGO−CH MODEL.

Kernel	FWHM$_{Fast}$ (ps)	FWHM$_{Slow}$ (ps)	Abundance Ratio
1	179.8	660.3	0.594
2	193.3	749.9	0.547
3	208.7	784.5	0.527
4	212.8	758.0	0.521
5	224.3	829.5	0.521
6	201.8	772.0	0.575
7	198.2	765.2	0.491
8	214.4	790.4	0.472
9	210.5	776.7	0.446
10	211.4	769.4	0.414
11	209.1	816.8	0.537
12	217.0	817.6	0.486
13	213.8	781.1	0.427
14	233.9	822.5	0.437
15	211.8	791.4	0.385
16	211.8	791.4	0.501
17	229.7	830.1	0.478
18	227.8	822.0	0.421
19	239.5	824.5	0.421
20	257.2	876.1	0.446
21	220.5	817.9	0.501
22	236.6	836.0	0.455
23	240.0	861.9	0.427
24	242.0	879.5	0.419
25	263.8	897.3	0.419

background activity 11.38 kBq/cc (42 MBq total activity), and hot spheres ratio 4:1. The source emitted back-to-back photons. The two larger spheres were made of water without activity. The simulated acquisition time was 150 s for all models. We considered one bed position without the scatter cylinder. We did not include a bed in the simulations. The phantom spheres were surrounded by a cold region representing the container's wall; the inner diameter of the spheres was $10-, 13-, 17-, 22-, 28-$ and 37 mm.

In order to compare the performance of the multiple mixture kernels with the single typical Gaussian kernels, using similar number of events, a complementary dataset (BGO−mCh−low), was generated as a subset of BGO−mCh events.

C. Image Reconstruction Toolkit

Software for Tomographic Image Reconstruction (STIR) (v.4.0) [45], [46] supports a wide range of reconstruction algorithms for the determination of the Maximum Likelihood Estimation (MLE). In this paper, we used TOF Listmode Maximum Likelihood-Expectation Maximisation (LM-MLEM) as it is the most robust option and is guaranteed to converge to a solution [47]–[49]. The validation of the TOF reconstruction with Gaussian [49]–[51] and non-Gaussian [52] kernels, has been presented in detail previously. In this study, the application of the TOF kernel is done in a similar manner to that of the simple Gaussian. In brief, the non-TOF Line-of-Response (LOR) (p_{ij}) is calculated and then the timing kernel is applied as:

$$p_{it;jp} = p_{ij} K_{it;jp}, \tag{1}$$

$$\begin{aligned} K_{it;jp} \quad &= (1-\alpha_p)(\mathrm{cdf}(k_{t+1} - v'_{cj}) - \mathrm{cdf}(k_t - v'_{cj}))_p + \\ &\alpha_p(\mathrm{cdf}(k_{t+1} - v'_{cj}) - \mathrm{cdf}(k_t - v'_{cj}))_p \end{aligned} \tag{2}$$

where $K_{it;jp}$ is the time response for the t^{th} TOF position of the i^{th} bin and j^{th} image element, cdf is the cumulative distribution function (CDF) corresponding to the timing kernel, $[k_t, k_{t+1})$ is the timing interval for the t^{th} TOF bin and v'_{cj} is the projection of the voxel's centre on the TOF line. The addition is the p which denotes the timing kernel for the particular event (1 to 25) and α_p is the corresponding abundance ratio between the two components (Ratio F/S in Table I).

1) Image Reconstruction: The reconstruction was performed for 150 iterations, although most discussion and analysis was focused on the 40^{th} iteration, which has been used for Siemens Biograph Vision [53], evaluation and is an acceptable choice in the clinic.

An image grid of $320 \times 320 \times 95$ voxels with size $1 \times 1 \times 2.08$ mm^3, was used. The size of the TOF bin was set to 1 ps. No TOF mashing, view mashing or axial compression, was used at the data. Furthermore, post-filtering was not applied on the reconstructed images.

The attenuation correction factors were calculated with an analytical projection of a digital representation of the emission phantom, having the appropriate linear attenuation values for 511 keV γ-photons, as found in NIST [54]. Post reconstruction, the images were calibrated to units of activity concentration (kBq/cc), by scaling the mean background value of the 150^{th} iteration.

The performance of background correction methods can vary widely [55], and the detectors under consideration are novel and in many aspects, unique. Therefore, in this study, we focused on demonstrating the potential benefits of the multiple timing kernels and higher sensitivity, using only true coincidences.

2) Reconstruction models: We reconstructed the simulated data using six different models. The simulation with the multiple mixture Gaussian spreads was reconstructed using the same 25 Mixture kernels (BGO−mCh), as summarised in Table I. The simulation with the single mixture Gaussian spread (BGO−Ch) was reconstructed with two different approaches. In the first approach we used a mixture kernel (BGO−Ch−mix). In the second case we used the exact mixture component that was applied, during the simulation, in each coincidence pair (columns 3 or 4 Table I). Essentially, we decompose the mixture kernel in two simple Gaussian kernels (BGO−Ch−dcmp). It has been suggested in the literature that the use of mixture kernels is not optimal. Whenever possible simple Gaussian kernels should be used [56]. The LYSO scanner was simulated with a typical Gaussian spread, therefore a typical Gaussian kernel (213 ps FWHM) was used in the reconstruction. Finally, for comparison we include a nonTOF reconstruction. All simulation cases and the reconstruction models, are summarised in Fig. 2.

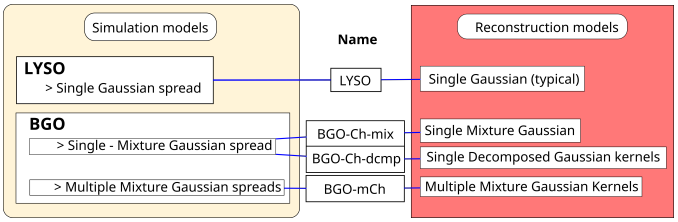

Fig. 2. Overview of the simulation and reconstruction models. The single mixture Gaussian spread used the first values from the first row of Table I.

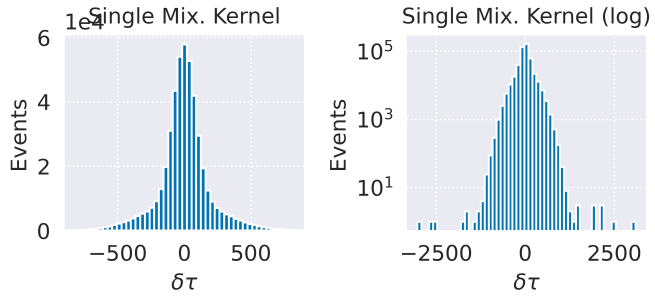

Fig. 3. Demonstration of the simulated time differences, using the modified GATE toolkit. The source was a point in the centre of the FOV. (left) time distribution from a single mixture Gaussian kernel (13th row) of Table I, (right) same on a log-scale.

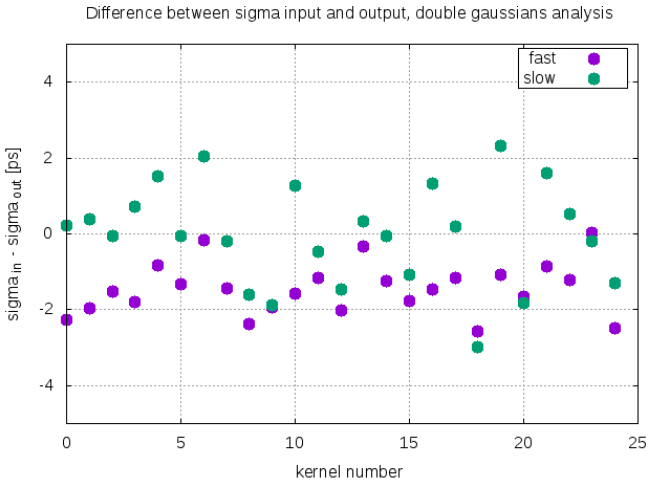

Fig. 4. Difference between simulated and experimental sigma of each of the 25 timing categories at Table I.

D. ROI selection and Figures of Merit

In the calculation of CRC and Background Variability (BV) we followed the NEMA guidelines on [44]. In brief, for each sphere (r) we drew circular Region-of-Interest (ROI)'s, on the central phantom slice, having the same diameter as the sphere. We sampled the background with 60 equally sized Regions-of-Interest (ROIs) for each sphere. The same ROIs were used for the presentation of the Standard Error (S.E.) and ROI mean value.

We evaluated the CNR following the methodology suggested previously [57] using the ROIs from the contrast calculation and the following formula:

$$\mathrm{CNR}_r = \frac{\mu_{H,r} - \mu_{B,r}}{\sqrt{\sigma^2_{H,r} + \sigma^2_{B,r}}} \tag{3}$$

where $\mu_{H,r}$ is mean values of a circular ROI, over sphere r, μ_{B_r} and $sigma_{B,r}$ are the mean value and average SD at the associated background regions.

The bias from each reconstruction method is estimated according to a methodology adapted from literature [58]. In this section, each ROI has half the diameter of the corresponding sphere, in order to avoid the partial volume effects. Each ROI's statistics were calculated across the multiple noise realisations and are compared to the expected activity concentration.

III. Results

A. Accuracy of Simulation and Statistics

On Fig. 3 we demonstrate the simulated time difference histogram of a point source placed in the centre of the Field-of-View (FOV), for one of the simulation repetitions. The above simulation used only the timing properties of row 13 of Table I.

Fig. 4 shows the difference between the sigma of the experimentally measured kernels (input) and the simulated (output) for every row of Table I. The data show that the simulated timing kernels are in good agreement with the experimental. There is an approximately ± 2 ps error which can be attributed to the statistics of the simulation.

With the NEMA phantom, the BGO model recorded on average 69.2×10^6 coincidences. The ratios Trues/Prompts, Randoms/Prompts and Scattered/Trues were 56.92%, 19.67% and 41.1%, respectively. The LYSO model recorded 38.0×10^6 coincidences and the corresponding ratios were 67.9%, 10.4% and 31.76%. The above ratios clearly demonstrate the negative impact of the BGO's energy resolution and larger coincidence window.

However, for the image reconstruction we used only true events. The BGO model recorded about 34% more true coincidences than LYSO; 39.37×10^6, 39.37×10^6 and 25.88×10^6 for the multiple kernel, the single kernel BGO (and the non TOF) and the LYSO models, respectively. The complementary `BGO-mCh-low` dataset had on average 26.27×10^6 true events.

We did not observe a significant difference in the total number of detected or true events between repetitions. We should note that multiple coincidences were left out of the simulation, as our multiple timing resolutions approach could potentially lead to the application of different timing spreads on pairs sharing one common `single` event, e.g. the same single being classified as fast for one pair and slow for another pair.

B. Mean value and Standard Error

On Figure 5 the mean value and S.E. of each hot sphere and all TOF models, are presented. We see that spheres converge in different iteration for each reconstruction model. The 22 mm sphere achieved its maximum value on the 80^{th}, 61^{th} and 54^{th} and 37^{th} for the `BGO-mCh`, the `BGO-Ch-mix`, the

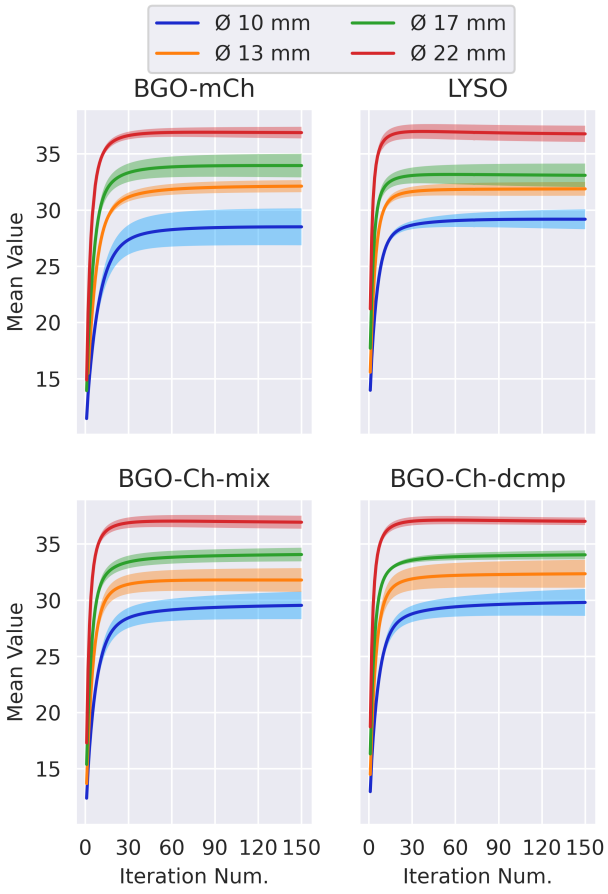

Fig. 5. Mean value of the four hot spheres for every Time-of-Flight model. The error bars are standard error over the five noise realisations. The BGO-Ch-mix and BGO-Ch-dcmp were reconstructed from the same dataset. BGO-mCh-low is a subset of BGO-mCh, with count number similar to LYSO.

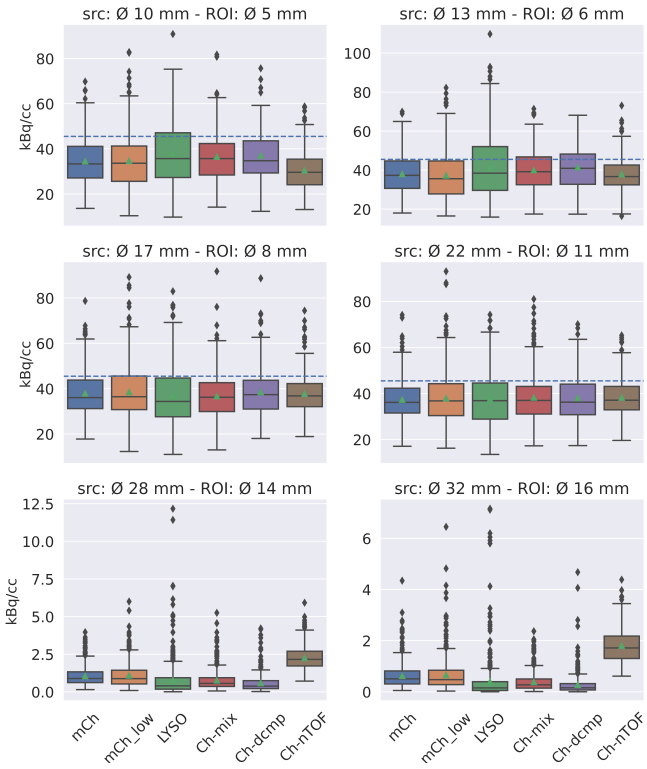

Fig. 6. Distribution of activity concentration values from the central part of all spheres in the NEMA-IQ phantom on the 40^{th} iteration and across five noise realisations. The expected activity concentration is indicated with a horizontal line.

`BGO-Ch-dcmp` and `LYSO` cases, respectively. The results show that the single Gaussian model converges to the maximum value sooner than the more complex models. In addition, the use of the exact component Gaussian kernel (`BGO-Ch-dcmp`) achieves convergence earlier than the use of the mixture model (`BGO-Ch-mix`).

The `BGO-Ch-mix` and `BGO-Ch-dcmp`, which shared the same simulated dataset, showed that the decomposition of the mixture kernel provided smaller S.E. at the two larger spheres and higher mean value for the smaller sphere. However, the later perfomed worse with the 13 mm sphere in terms of S.E..

Overall, the complexity of the timing model seems to have a negative impact to the convergence. `BGO-Ch-mix`, in most cases has smaller S.E. than `BGO-mCh`, `BGO-Ch-dcmp` converges faster than `BGO-Ch-mix`. However, the differences between them are not strong.

C. ROI statistics

On Figure 6 the distribution of voxel values for the central part of each ROI, across all five noise realisations, on the 40^{th} iteration, is summarised. We see that reconstruction with single Gaussian (`LYSO`) yields smaller value density compared to single or multiple mixture kernels, even for a similar amount of events. The above observation is more prominent for the smaller sources. However, the median values are similar. It is worth noting that in some spheres the `LYSO` model had a right side skewed distribution, which other cases presented in a much lesser degree. This lead to the mean value of `LYSO` being closer to the expected.

Surprisingly, we cannot detect a significant difference, in terms of mean value, between the use of mixture and decomposed kernels. Although, the later has access to more information and in the previous paragraph we showed that it converges sooner. However, we see that it has lower value density, which indicates higher noise and maybe that it is further in the reconstruction process.

As expected, the `nonTOF` has the lowest mean value in the smaller spheres as it needs to be iterated more. Likewise, in the cold regions the nonTOF has the highest mean values. Here, we see the single Gaussian model to have the lowest median value and better mean value (closer to 0) than the models with multiple mixture kernels. Moreover, the decomposed model showed denser value distribution and better mean and median values, than the mixture model.

On figure 7 we demonstrate the reconstructed central slice and associated line profiles (average of five rows) of all cases on the 40^{th} iteration, from one of the noise realisations. One can see the increased noise in `LYSO` (background and source) and possibly notice a slightly noisier `BGO-Ch-dcmp` in comparison to the `BGO-Ch-mix`.

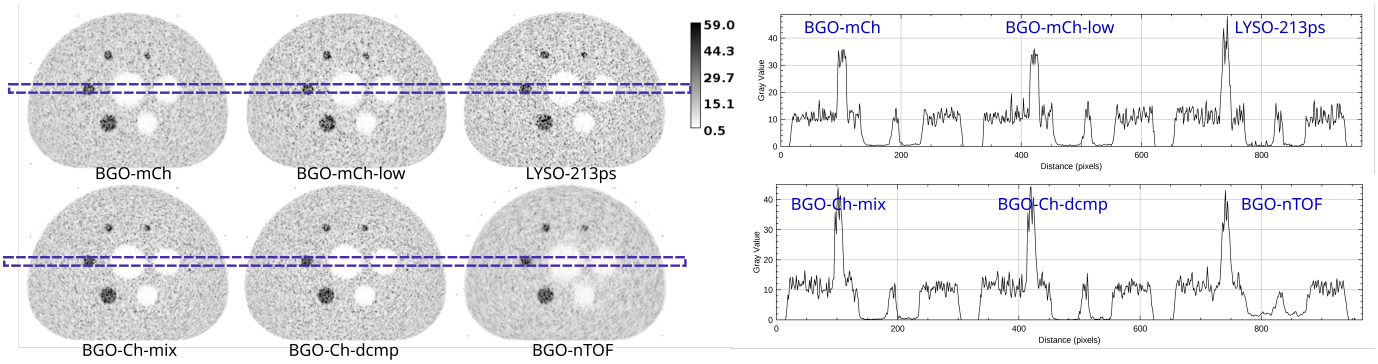

Fig. 7. Reconstructed images at the 40^{th} iteration for the different detector models for one of the noise realisations.

D. Contrast Recovery

Figure 8 shows the average contrast recovery ($\overline{CRC}$) against the average background variability ($\overline{BV}$), of the five noise realisations. The markers on the curves indicate the iterations with number 1, 2, 3, 4, 5, 10, 20, 40, 80 and 150.

Noteworthy is the reduction in $\overline{BV}$ that takes place in the first five iterations for the complex timing models. The above behaviour is more prominent to the `BGO-mCh`, and to a lesser degree to `BGO-Ch-mix` and `BGO-Ch-dcmp`. Also, the recovery of the mixture-kernels reconstruction during the first iterations is quite lower than of the single kernel model. Result of this *"slow start"* is that the mixture-kernel convergence step is larger, during iterations between 10 and 40, than that of the regular TOF reconstruction. In most cases, the mixture-kernels' $\overline{CRC}$ reaches a similar level with the single-kernel, by the 40^{th}. For similar number events (comparison between `LYSO` and `BGO-mCh-low`) at the 40^{th} iteration the $\overline{BV}$ is comparable. However, at later iterations the simple Gaussian model manages noise more efficiently.

Comparison of the `Ch-mix` and `Ch-dcmp` models (which use the same datasets) shows that using the decomposed kernel benefits the contrast recovery during early iterations. However, at after the 30^{th} iteration the mixture model has similar recovery, with slightly better $\overline{BV}$.

E. Contrast-to-Noise ratio

Investigating the $\overline{CNR}$ iteration-after-iteration, we can see that the higher sensitivity of the BGO scanner has a strong positive impact (Figure 9). We report up to 22.79% higher $\overline{CNR}$ for the 22 mm sphere and about 26.40% for the 13 mm. The `BGO-mCh-low` performed in-between the `BGO-mCh` and `LYSO` models, depending on the size of the source. The difference in the performance of the `BGO-mCh-low` can be explained by the high S.E. that some sources showed (Fig. 5).

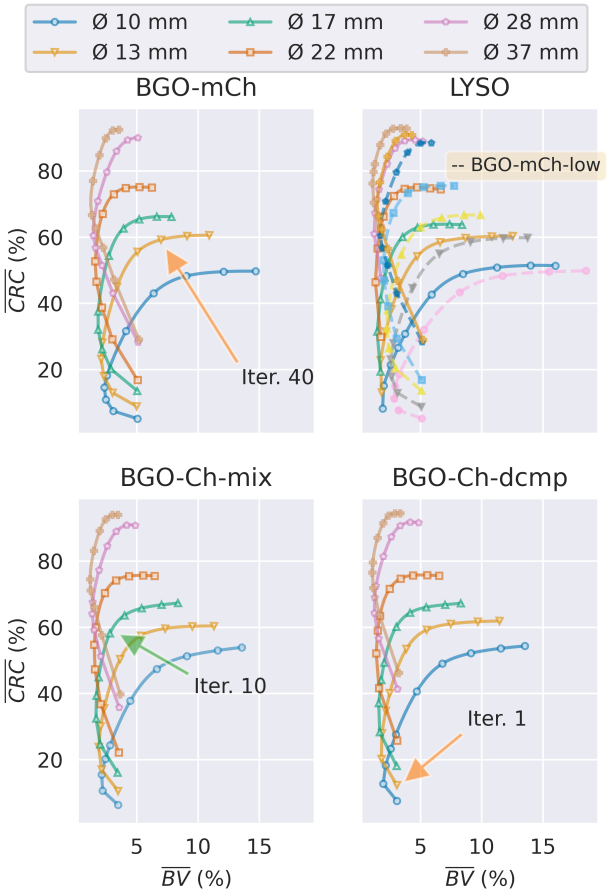

Fig. 8. Contrast Recovery Coefficient for every hot and cold ROI in the NEMA phantom for the BGO-mCh and LYSO (213 ps) models. Along side the LYSO model with dashed lines the low count BGO-mCh-low, is presented. The markers annotate iteration numbers: 1, 2, 3, 4, 5, 10, 20, 40, 80 and 150.

IV. Discussion

In this paper, we presented the validation and initial evaluation of a Monte Carlo framework for the statistical simulation of data modelled for detectors that produce multiple time resolutions. In this instance, we used the framework to investigate the performance of BGO-Cherenkov detectors which were modelled after the experimental measurements. Also, we investigated the effect of multiple TOF kernels in the PET image quality.

We based the MC simulation framework on the GATE toolkit that we appropriately modified. The simulation does not model individual optical photons and their propagation. Instead, it takes a statistical approach and applies multiple timing spreads on the coincidences, per the experimental data. Previously we demonstrated that an appropriate model for the BGO-Cherenkov detectors is that of multiple mixture Gaussian

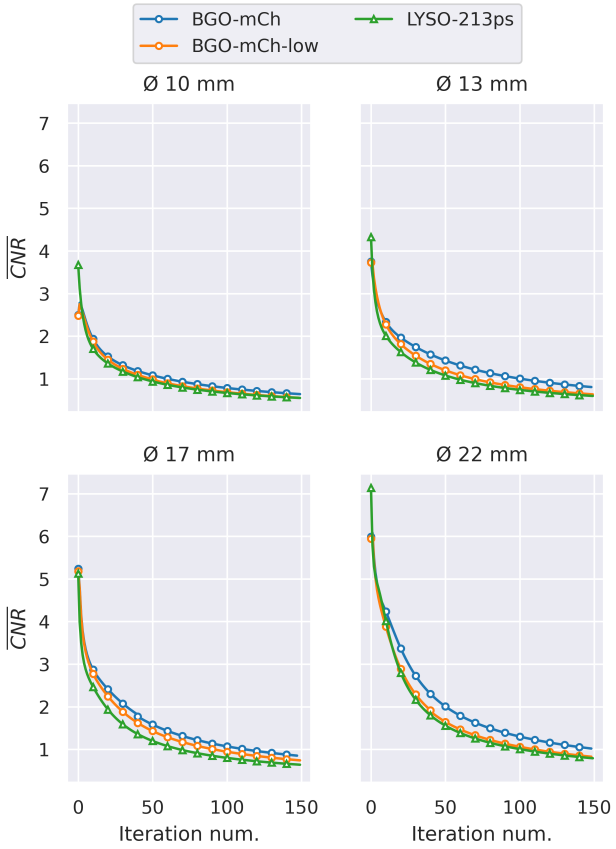

Fig. 9. Contrast-to-Noise ratio for all hot spheres of the NEMA phantom using the BGO-mCh with high and low number of events and a single Gaussian model with LYSO.

kernels. The different kernels account for different proportions of Cherenkov photons detected alongside the normal BGO scintillation light.

In this investigation, we modelled a generic cylindrical PET scanner and the NEMA IQ phantom. Simulated timing histograms from a point source in the centre of the FOV showed excellent agreement with the experiments (± 2 ps). The repeated simulations with the NEMA-IQ phantom showed that due to its high density, the BGO crystal measured approx. 34% more coincidences than LYSO. However, had poorer scattered ratio, due to the low energy resolution. In the activity level of this investigation the difference on randoms was not large.

Comparison between a the `BGO-mCh` model (BGO detectors, multiple mixture kernels) with the `LYSO` (single Gaussian kernel) showed that the former is able to achieve similar CRC (after the 40^{th} iteration) with lower BV. The advantages of the higher stopping power are demonstrated in terms of CNR with an improvement of 26.4%. The smaller standard deviation (not shown here) in the ROIs using BGO can offer a better estimation of SUVmax.

For comparable number of events (case of `BGO-mCh-low`) the simple Gaussian kernel performed better, in terms of contrast at iterations below 40^{th} and, in terms of noise after the 70^{th} (subject to the size of the sphere). Having that said, the difference was not strong. Therefore the use BGO detectors with TOF can lead the way to even lower administered doses or smaller acquisition time.

Comparison between `BGO-Ch-mix` and `BGO-Ch-dcmp`, showed that the use of the exact timing model offers better performance in terms of mean value and standard error. However, second order metrics (i.e. CRC and BV) did not show strong differences.

As a general comment on the complexity of the timing model, we can state that it has a negative effect on the performance of MLEM. Maybe categorising the events in less categories could have some advantages. However, it is a *price worth paying* for the higher sensitivity.

This study has several limitations, which have been discussed through-out the manuscript. In summary, full BGO scanners with fast acquisition electronics have not been manufactured in the past, therefore we did not had a precedent to base our simulation model on. In order to confirm the used energy resolution of BGO we performed an dedicated light yield measurement with ^{137}Cs and a PMT from Hamamatsu (R 2059) and measure an energy resolution of 17.3 % for 2x2x20 mm^3 crystal geometry. Scaling this value down to 511 keV leads to an energy resolution of 19.6 %. However, we are not yet in a position to predict accurately the potential performance characteristics of a full BGO-Cherenkov PET scanner and therefore the inclusion of background radiation would not had been helpful. In this initial study we focused on reconstruction of true events only, which limits the presented findings to a certain aspect. Other effects as dead-time / pile-up will probably have to be addressed in a full scanner as well.

A final point which has not been discussed in-detail, is illustrated in Fig 1; the mean value of the measured timing distributions is not centred at zero. This happens as the two pulses may not pass the lower threshold at the same time due to different rise times. In this investigation, we did not consider this shift in the simulation, we set the simulated kernels to be centred. A correction algorithm, similar to the TOF bin time shift, would have to be developed and applied in the real scanner/detector systems.

V. Conclusion

In this paper we presented validation and initial performance evaluation of a framework that can be used to simulate and reconstruct data from PET scanner geometries, modelling BGO-Cherenkov detectors. The reconstruction takes into account the multiple timing resolutions as provided by Cherenkov detectors, with 25 timing kernels ranging from 180 ps to 263 ps. Initial results with these mixture Gaussian kernels showed promising characteristics, as it performed *on par* with a 213 ps typical single Gaussian model in terms of Contrast Recovery but with better Background Variability. In addition, we showed that BGO-Cherenkov detectors, if corrected for background, can provide improved Contrast-to-Noise ratio.

References

[1] T. Jones *et al.*, "History and future technical innovation in positron emission tomography," *Journal of Medical Imaging*, vol. 4, no. 1, p. 011 013, Mar. 2017, ISSN: 2329-4302. DOI: 10.1117/1.jmi.4.1.011013.

[2] T. Tomitani, "Image reconstruction and noise evaluation in photon Time-of-Flight assisted Positron Emission Tomography," *IEEE Trans. Nucl. Sci.*, vol. NS-28, no. 6, pp. 4581–4589, 1981.

[3] D. L. Snyder *et al.*, "Image reconstruction from list-mode data in an emission tomography system having time-of-flight measurements," *IEEE Trans. Nucl. Sci.*, vol. 30, no. 3, pp. 1843–1849, 1983. DOI: 10.1109/TNS.1983.4332660.

[4] N. A. Mullani *et al.*, "Dynamic imaging with high resolution Time-of-Flight PET camera - TOFPET I," *IEEE Trans. Nucl. Sci.*, vol. 31, no. 1, pp. 609–613, 1984. DOI: 10.1109/TNS.1984.4333329.

[5] D. L. Snyder, "A mathematical model for Positron-Emission Tomography systems having Time-of-Flight measurements," *IEEE Trans. Nucl. Sci.*, vol. 75, no. 3, 1981. DOI: 10.1109/TNS.1981.4332168.

[6] J. S. Karp *et al.*, "Benefit of Time-of-Flight in PET: experimental and clinical results.," *J. Nucl. Med.*, vol. 49, no. 3, pp. 462–70, 2008. DOI: 10.2967/jnumed.107.044834.

[7] D. J. Kadrmas *et al.*, "Impact of time-of-flight on PET tumor detection.," *Journal of nuclear medicine : official publication, Society of Nuclear Medicine*, vol. 50, no. 8, pp. 1315–1323, 2009, ISSN: 0161-5505. DOI: 10.2967/jnumed.109.063016. [Online]. Available: http://www.pubmedcentral.nih.gov/articlerender.fcgi?artid=2786272&tool=pmcentrez&rendertype=abstract.

[8] S. Surti *et al.*, "Impact of time-of-flight PET on whole-body oncologic studies: A human observer lesion detection and localization study," *Journal of Nuclear Medicine*, vol. 52, no. 5, pp. 712–719, May 2011, ISSN: 01615505. DOI: 10.2967/jnumed.110.086678. [Online]. Available: http://jnm.snmjournals.org/content/52/5/712.full%20http://jnm.snmjournals.org/content/52/5/712.abstract.

[9] G. El Fakhri *et al.*, "Improvement in lesion detection with whole-body oncologic time-of-flight PET," *Journal of Nuclear Medicine*, vol. 52, no. 3, pp. 347–353, 2011, ISSN: 01615505. DOI: 10.2967/jnumed.110.080382.

[10] E. Clementel *et al.*, "Evaluation of Image Signal-to-Noise Ratio in Time-of-flight PET," *IEEE Nucl. Sci. Symp. Conf. Rec.*, pp. 3917–3921, 2011.

[11] S. Surti, "Update on time-of-flight PET imaging.," *Journal of nuclear medicine : official publication, Society of Nuclear Medicine*, vol. 56, no. 1, pp. 98–105, 2015. DOI: 10.2967/jnumed.114.145029.

[12] L. Presotto *et al.*, "Evaluation of image reconstruction algorithms encompassing Time-Of-Flight and Point Spread Function modelling for quantitative cardiac PET: Phantom studies," *J. Nucl. Cardiol.*, vol. 22, no. 2, pp. 351–363, Apr. 2015. DOI: 10.1007/s12350-014-0023-1.

[13] S. Vandenberghe *et al.*, "Recent developments in time-of-flight PET," *EJNMMI Physics*, vol. 3, no. 1, p. 3, Dec. 2016. DOI: 10.1186/s40658-016-0138-3.

[14] D. R. Schaart *et al.*, "LaBr ¡sub¿3¡/sub¿ :Ce and SiPMs for time-of-flight PET: achieving 100 ps coincidence resolving time," *Physics in Medicine and Biology*, vol. 55, no. 7, N179–N189, Apr. 2010, ISSN: 0031-9155. DOI: 10.1088/0031-9155/55/7/N02. [Online]. Available: https://iopscience.iop.org/article/10.1088/0031-9155/55/7/N02.

[15] P. Lecoq, "Pushing the Limits in Time-of-Flight PET Imaging," *IEEE Trans. Rad. Plasma Med. Sci.*, vol. 1, no. 6, pp. 473–485, Nov. 2017. DOI: 10.1109/TRPMS.2017.2756674.

[16] J. W. Cates *et al.*, "Evaluation of a clinical TOF-PET detector design that achieves," *Phys. Med. Biol.*, vol. 63, no. 11, p. 115011, Jun. 2018. DOI: 10.1088/1361-6560/aac504.

[17] D. Schaart *et al.*, "Achieving 10 ps coincidence time resolution in TOF-PET is an impossible dream," *Med Phys*, 2020. DOI: 10.1002/mp.14122.

[18] C. Tsoumpas, "Why ultrafast is ultra-good," *Physics World*, 2020.

[19] P. Lecoq *et al.*, "Roadmap toward the 10 ps time-of-flight PET challenge," *Physics in Medicine & Biology*, 2020, ISSN: 0031-9155. DOI: 10.1088/1361-6560/ab9500. [Online]. Available: https://doi.org/10.1088/1361-6560/ab9500.

[20] W. W. Moses *et al.*, "Prospects for Time-of-Flight PET using LSO scintillator," *IEEE Trans. Nucl. Sci.*, vol. 46, pp. 474–478, 1999. DOI: 10.1109/23.775565.

[21] C. Melcher *et al.*, "Cerium-doped lutetium oxyorthosilicate: a fast, efficient new scintillator," *IEEE Trans. Nucl. Sci.*, vol. 39, no. 4, pp. 502–505, 1992. DOI: 10.1109/23.159655.

[22] R. Nutt *et al.*, "Is LSO the future of PET?" Tech. Rep. 11, Nov. 2002, pp. 1523–1528. DOI: 10.1007/s00259-002-0987-y. [Online]. Available: http://www.deepdyve.com/lp/springer-journals/is-lso-the-future-of-pet-ZPDAV340O4%20http://www.deepdyve.com/lp/springer-journals/is-lso-the-future-of-pet-ZPDAV340O4.

[23] M. Conti *et al.*, "First experimental results of Time-of-Flight reconstruction on an LSO PET scanner.," *Phys. Med. Biol.*, vol. 50, no. 19, pp. 4507–26, 2005. DOI: 10.1088/0031-9155/50/19/006.

[24] S. Surti *et al.*, "Performance of Philips Gemini TF PET/CT scanner with special consideration for its time-of-flight imaging capabilities.," *J. Nucl. Med.*, vol. 48, no. 3, pp. 471–480, Mar. 2007.

[25] C. L. Melcher, "Scintillation crystals for PET.," *J. Nucl. Med.*, vol. 41, no. 6, pp. 1051–5, Jun. 2000.

[26] M. Miyata *et al.*, "Development of TOF-PET using Cherenkov Radiation," *J Nucl Sci Tech*, vol. 43, no. 4, pp. 339–343, Apr. 2006. DOI: 10.1080/18811248.2006.9711101.

[27] S. Korpar *et al.*, "Study of TOF PET using Cherenkov light," *Nuclear Instruments and Methods in Physics Research Section A: Accelerators, Spectrometers, Detectors and Associated Equipment*, vol. 654, no. 1, pp. 532–538, Oct. 2011. DOI: 10.1016/j.nima.2011.06.035.

[28] S. E. Brunner *et al.*, "Studies on the {Cherenkov} Effect for Improved Time Resolution of {TOF-PET}," *IEEE Transactions on Nuclear Science*, vol. 61, no. 1, pp. 443–447, Feb. 2014, ISSN: 0018-9499. DOI: 10.1109/TNS.2013.2281667.

[29] E. Roncali *et al.*, "Cerenkov light transport in scintillation crystals explained: Realistic simulation with GATE," *Biomedical Physics and Engineering Express*, vol. 5, no. 3, p. 035033, Apr. 2019, ISSN: 20571976. DOI: 10.1088/2057-1976/ab0f93. [Online]. Available: https://iopscience.iop.org/article/10.1088/2057-1976/ab0f93%20https://iopscience.iop.org/article/10.1088/2057-1976/ab0f93/meta.

[30] S. E. Brunner *et al.*, "BGO as a hybrid scintillator / Cherenkov radiator for cost-effective time-of-flight PET," *Phys. Med. Biol.*, vol. 62, no. 11, pp. 4421–4439, Jun. 2017. DOI: 10.1088/1361-6560/aa6a49.

[31] G. Borghi *et al.*, "BGO as a hybrid scintillator / Cherenkov radiator for cost-effective time-of-flight PET Initial PET performance evaluation of a preclinical insert for PET/MRI with digital SiPM technology BGO as a hybrid scintillator / Cherenkov radiator for cost-effectiv," *Schaart Phys. Med. Biol*, vol. 62, 2017. DOI: https://doi.org/10.1088/1361-6560/aa6a49.

[32] M. Alokhina *et al.*, "Simulation and optimization of the Cherenkov TOF whole-body PET scanner," *Nuclear Instruments and Methods in Physics Research Section A: Accelerators, Spectrometers, Detectors and Associated Equipment*, vol. 912, pp. 378–381, Dec. 2018. DOI: 10.1016/j.nima.2018.01.027.

[33] R. Ota *et al.*, "Timing-performance evaluation of Cherenkov-based radiation detectors," *Nuclear Instruments and Methods in Physics Research Section A: Accelerators, Spectrometers, Detectors and Associated Equipment*, vol. 923, pp. 1–4, Apr. 2019. DOI: 10.1016/J.NIMA.2019.01.034.

[34] S. I. Kwon *et al.*, "Bismuth germanate coupled to near ultraviolet silicon photomultipliers for time-of-flight PET," *Physics in Medicine and Biology*, vol. 61, no. 18, pp. L38–L47, Sep. 2016, ISSN: 13616560. DOI: 10.1088/0031-9155/61/18/L38. [Online]. Available: https://iopscience.iop.org/article/10.1088/0031-9155/61/18/L38%20https://iopscience.iop.org/article/10.1088/0031-9155/61/18/L38/meta.

[35] N. Kratochwil *et al.*, "Pushing Cherenkov PET with BGO via coincidence time resolution classification and correction - IOPscience," *Phys. Med. Biol*, 2020. [Online]. Available: https://iopscience.iop.org/article/10.1088/1361-6560/ab87f9.

[36] N. Kratochwil *et al.*, "Exploring Cherenkov emission of BGO for TOF-PET," *IEEE Transactions on Radiation and PlasmaMedical Sciences (under consideration)*,

[37] P. Cherenkov, "Visible emission of clean liquids by action of γ radiation," *Dokl. Adad. Nauk SSSR*, vol. 451, 1934.

[38] S. Gundacker *et al.*, "Experimental time resolution limits of modern SiPMs and TOF-PET detectors exploring different scintillators and Cherenkov emission," *Physics in Medicine & Biology*, vol. 65, no. 2, p. 25 001, 2020, ISSN: 1361-6560. DOI: 10.1088/1361-6560/ab63b4. [Online]. Available: http://10.0.4.64/1361-6560/ab63b4%20https://dx.doi.org/10.1088/1361-6560/ab63b4.

[39] S. Gundacker *et al.*, "Measurement of intrinsic rise times for various {L(Y)SO} and {LuAG} scintillators with a general study of prompt photons to achieve 10 ps in {TOF-PET}," *Physics in Medicine & Biology*, vol. 61, no. 7, p. 2802, 2016. [Online]. Available: http://stacks.iop.org/0031-9155/61/i=7/a=2802.

[40] J. Van Sluis *et al.*, "Performance characteristics of the digital biograph vision PET/CT system," *Journal of Nuclear Medicine*, vol. 60, no. 7, pp. 1031–1036, 2019, ISSN: 2159662X. DOI: 10.2967/jnumed.118.215418.

[41] M. E. Casey *et al.*, "Siemens Biograph Vision 600," in *Advances in PET*, Springer International Publishing, 2020, pp. 71–91. DOI: 10.1007/978-3-030-43040-5{_}6. [Online]. Available: https://link.springer.com/chapter/10.1007/978-3-030-43040-5_6.

[42] S. Gundacker *et al.*, "High-frequency {SiPM} readout advances measured coincidence time resolution limits in {TOF-PET}," *Physics in Medicine & Biology*, vol. 64, no. 5, p. 55 012, 2019. DOI: 10.1088/1361-6560/aafd52. [Online]. Available: http://doi.org/10.1088/1361-6560/aafd52.

[43] S. Jan *et al.*, "GATE : a simulation toolkit for PET and SPECT," *Physics in Medicine and Biology*, vol. 49, no. 19, pp. 4543–4561, Oct. 2004, ISSN: 00319155. DOI: 10.1088/0031-9155/49/19/007.

[44] National Electrical Manufacturers Association, *Performance measurements of positron emission tomographs. NEMA Standards Publication NU 2-2012*. 2012.

[45] K. Thielemans *et al.*, "STIR: Software for tomographic image reconstruction release 2," *Phys. Med. Biol*, vol. 57, no. 4, pp. 867–883, Feb. 2012, ISSN: 00319155. DOI: 10.1088/0031-9155/57/4/867.

[46] E. Ovtchinnikov *et al.*, "SIRF: Synergistic Image Reconstruction Framework," *Computer Physics Communications*, p. 107 087, Dec. 2019. DOI: 10.1016/J.CPC.2019.107087.

[47] L. A. Shepp *et al.*, "Maximum likelihood reconstruction for Emission Tomography," *IEEE Trans. on Med. Imag.*, vol. 1, no. 2, pp. 113–122, Oct. 1982. DOI: 10.1109/TMI.1982.4307558.

[48] H. H. Barrett *et al.*, "List-mode likelihood," *J. Opt. Soc. Am.*, vol. 14, no. 11, pp. 2914–2923, 1997, ISSN: 1084-7529. DOI: 10.1364/JOSAA.14.002914.

[49] N. Efthimiou *et al.*, "Implementation and validation of time-of-flight PET image reconstruction module for listmode and sinogram projection data in the STIR library," *Physics in Medicine and Biology*, vol. 64, no. 3, 2019, ISSN: 13616560. DOI: 10.1088/1361-6560/aaf9b9.

[50] J. Renner *et al.*, "Processing of Compton events in the PETALO readout system," 2019.

[51] P. Wadhwa *et al.*, "PET image reconstruction using physical and mathematical modelling for time of flight PET-MR scanners in the STIR library," *Methods*, Jan. 2020, ISSN: 10462023. DOI: 10.1016/j.ymeth.2020.01.005. [Online]. Available: https://linkinghub.elsevier.com/retrieve/pii/S1046202319301938.

[52] N. Efthimiou *et al.*, "Use of non-Gaussian time-of-flight kernels for image reconstruction of Monte Carlo simulated data of ultra-fast PET scanners," *EJNMMI Physics*, vol. 7, no. 1, p. 42, Dec. 2020, ISSN: 21977364. DOI: 10.1186/s40658-020-00309-8.

[53] M. E. Casey *et al.*, "Advances in PET," *Advances in PET*, 2020. DOI: 10.1007/978-3-030-43040-5.

[54] J. Hubbell *et al.*, "Tables of x-ray mass attenuation coefficients and mass energy-absorption coefficients 1 keV to 20 meV for elements z = 1 to 92 and 48 additional substances of dosimetric interest," National Inst. of Standards and Technology, PL, Gaithersburg, MD (United States), Tech. Rep., May 1995.

[55] H. Zaidi *et al.*, "Scatter modelling and compensation in emission tomography," *European Journal of Nuclear Medicine and Molecular Imaging*, vol. 31, no. 5, pp. 761–782, May 2004, ISSN: 16197070. DOI: 10.1007/s00259-004-1495-z.

[56] X. Zhuang *et al.*, "Gaussian mixture density modeling, decomposition, and applications," *IEEE Transactions on Image Processing*, vol. 5, no. 9, pp. 1293–1302, 1996, ISSN: 10577149. DOI: 10.1109/83.535841.

[57] D. Deidda *et al.*, "Hybrid PET-MR list-mode kernelized expectation maximization reconstruction," *Inverse Problems*, vol. 35, no. 4, 2019, ISSN: 13616420. DOI: 10.1088/1361-6420/ab013f.

[58] K. Van Slambrouck *et al.*, "Bias reduction for low-statistics PET: Maximum likelihood reconstruction with a modified poisson distribution," *IEEE Transactions on Medical Imaging*, vol. 34, no. 1, pp. 126–136, 2015, ISSN: 1558254X. DOI: 10.1109/TMI.2014.2347810.